PNAS RESEARCH ARTICLE | APPLIED PHYSICAL SCIENCES OPEN ACCESS

Linear resistivity at van Hove singularities in twisted bilayer WSe_2

LingNan Wei[a,1], Qiaoling Xu[b,c,1], Yangchen He[d], Qingxin Li[a], Yan Huang[a], Wang Zhu[a], Kenji Watanabe[e], Takashi Taniguchi[f], Martin Claassen[g], Daniel A. Rhodes[d], Dante M. Kennes[h,i,2], Lede Xian[b,i,2], Angel Rubio[i,j,2], and Lei Wang[a,k,2]

Contributed by Angel Rubio; received December 10, 2023; accepted March 8, 2024; reviewed by Massimo Capone, Xiaobo Lu, and Li Yang

Different mechanisms driving a linear temperature dependence of the resistivity $\rho \sim T$ at van Hove singularities (VHSs) or metal-insulator transitions when doping a Mott insulator are being debated intensively with competing theoretical proposals. We experimentally investigate this using the exceptional tunability of twisted bilayer (TB) WSe_2 by tracking the parameter regions where linear-in-T resistivity is found in dependency of displacement fields, filling, and magnetic fields. We find that even when the VHSs are tuned rather far away from the half-filling point and the Mott insulating transition is absent, the T-linear resistivity persists at the VHSs. When doping away from the VHSs, the T-linear behavior quickly transitions into a Fermi liquid behavior with a T^2 relation. No apparent dependency of the linear-in-T resistivity, besides a rather strong change of prefactor, is found when applying displacement fields as long as the filling is tuned to the VHSs, including $D \sim 0.28$ V/nm where a high-order VHS is expected. Intriguingly, such non-Fermi liquid linear-in-T resistivity persists even when magnetic fields break the spin-degeneracy of the VHSs at which point two linear in T regions emerge, for each of the split VHSs separately. This points to a mechanism of enhanced scattering at generic VHSs rather than only at high-order VHSs or by a quantum critical point during a Mott transition. Our findings provide insights into the many-body consequences arising out of VHSs, especially the non-Fermi liquid behavior found in moiré materials.

non-Fermi liquid behavior | van Hove singularity | twisted bilayer WSe_2 | correlated phenomena | ab initio electronic structure

Significance

Many quantum materials exhibit an intriguing strange metal phase, characterized by a linear in temperature resistivity. The relation of this phase to other emergent quantum many-body phases, such as superconductivity, triggers an intense debate to this date. Here, we study twisted bilayer (TB-) WSe_2 and report on the tunability of emergent phenomena driven by the high density of states caused by vanishing slopes in the dispersion relation: so-called Van Hove singularities (VHSs). We observe that linear in temperature resistivity closely follows the positions of the VHSs independent of the presence or absence of quantum criticality and seemingly agnostic of their high-order nature. Our findings establish TB-WSe_2 as a promising platform to investigate the relevance of VHSs for quantum materials.

The electrical resistivity of metallic states at low temperatures (T) exhibits T^2 dependence, which follows the Landau-Fermi liquid theory where the average relaxation time for electrons on the Fermi surface is inversely proportional to T^2 (1–4). There are a few marked exceptions in which the very general Fermi liquid behavior breaks down, for example, the unconventional high-T_c superconductors above T_c (5–10) and Mott insulators doped to their quantum critical points (11–13). In such systems, resistivity shows a linear T dependence, referred to as a strange metal (9, 10, 14, 15), a strongly correlated phenomenon that has not been yet well understood. Early considerations of van Hove singularities (VHSs) led to the idea that enhanced electron–electron or electron–phonon scattering might also led to linear in T resistivity (16, 17), however, at least for the electron–electron part, this scenario was not supported by a dynamical mean field analysis (18). Intriguingly, recent theories proposed that a T-linear behavior can also result from special, extended types of VHSs where the density of states (DOS) exhibits a power-law divergence in two-dimensional systems, known as high-order van Hove singularities (hVHSs) (19–22). Due to its pronounced divergence, an hVHS can also induce ordering instabilities and give rise to exotic correlated phenomena, including supermetal, ferromagnetism, and chiral superconductivity (20, 23–25).

High-order VHSs have been theoretically reported in various conventional systems before, like cuprate high-T_c superconductors (26, 27), $Sr_3Ru_2O_7$ (28), and bilayer graphene (19). However, a systematic transport experimental characterization of their properties was up to recently hindered by the lack of sufficiently controlled material platforms. With the advent of tunable moiré systems for which theory proposed the existence of hVHSs, there is a unique opportunity to investigate hVHSs, since the flat band in these systems has lower energy which enable us to access their band characteristics through transport measurements. Among the various theoretical predictions regarding moiré systems (21, 29–31), twisted homobilayer transition metal dichalcogenides (TMDs) systems have unique advantages, they feature spin-valley locking simplifying the band degeneracy to two, much simpler compared to twisted graphene systems. Moreover, in twisted homobilayer TMDs exist both conventional VHSs and high-order VHSs, with one type easily transitioning to the other by applying displacement fields, and allow for the exploration of hVHSs (29, 32, 33).

Reviewers: M.C., Scuola Internazionale Superiore di Studi Avanzati; X.L., Peking University; and L.Y., Washington University in St. Louis.

Competing interest statement: K.W. and T.T. are on multiple papers with reviewers due to their position as materials sources in this field. Because they provide hexagonal boron nitride to so many workers in the field, it is not feasible to find referees who are not co-authors with them.

Copyright © 2024 the Author(s). Published by PNAS. This open access article is distributed under Creative Commons Attribution License 4.0 (CC BY).

[1]L. Wei and Q.X. contributed equally to this work.

[2]To whom correspondence may be addressed. Email: dante.kennes@mpsd.mpg.de, xianlede@sslab.org.cn, angel.rubio@mpsd.mpg.de, or leiwang@nju.edu.cn.

This article contains supporting information online at https://www.pnas.org/lookup/suppl/doi:10.1073/pnas.2321665121/-/DCSupplemental.

Published April 9, 2024.

Downloaded from https://www.pnas.org by UKA AACHEN INTEGR. MEDIENBEARB. MEDIZIN on January 30, 2025 from IP address 134.130.130.179.

Recently, quantum critical behavior near half-filling correlated insulating state has been reported in 4.2° TB-WSe_2 device (13). However, under such a twisted angle, theory suggests that the VHS is also expected to appear right at the half-filling position where the Mott insulator exists (33) and that a hVHS point is nearby with respect to changing the displacement field. In this case, disentangling the property of the VHSs, hVHSs, and the Mott insulator physics can be challenging, as doping a Mott insulator to the quantum critical point can also induce a *T*-linear behavior of the resistivity. In this paper, we choose smaller twisted angles, for which the hVHSs are further away from the half-filling correlated insulating state. This allows to access the unperturbed VHSs and hVHSs physics and to tune in and out of the Mott regime. Thus, our work can shed light on the mechanism driving linear in *T* resistive behavior. We use the 'tear and stack' method (34–36) to fabricate multiple TB-WSe_2 devices with AA stacking order (37). This method combines prepatterned Hall bar-shaped Pt leads (38) (*SI Appendix*, Fig. S1) and a dual-gate structure to achieve a lower contact resistivity at low temperatures (39), similar to previous works (13, 40). Multiple devices show similar results. Here, we mainly focus on the 3.2° TB-WSe_2 device.

In Fig. 1*A*, the top panel shows an illustration of a TB-WSe_2 device with a dual-gate structure in which we can independently tune the displacement fields D and carrier density n (36, 40). The corresponding optical image of a real TB-WSe_2 device is displayed in the bottom panel. Schematic illustrations of the moiré superlattice in real space (*Top* panel) and reciprocal space (*Bottom* panel) are shown in Fig. 1*B*. We also calculate the band structure of TB-WSe_2 with a twist angle of 3.15° (*SI Appendix*, Fig. S2). Fig. 1*C* shows the longitudinal resistivity ρ as a function of the normalized carrier density n/n_s at a top gate voltage V_{tg} of −4.3 V and various temperatures. Here, n_s denotes populate one hole in each moiré unit cell. We can observe two prominent peaks, corresponding to a half-filling correlated state and a full-filling state, respectively. Notably, both peak values decrease with increasing temperature, confirming their insulating nature. Furthermore, we also observe that the half-filling peak exhibits asymmetric behavior at 1.5 K, which can be seen as the VHSs deviating slightly from half-filling position.

To investigate the tunability of the VHSs in TB-WSe_2, we measure the longitudinal resistivity ρ plotted against the normalized carrier density n/n_s at V_{tg} of −5.3 V, −6.3 V, −7.3 V, and −8.3 V, respectively, as shown in Fig. 2*A*. By applying a displacement field, we successfully achieve the tuning of the VHSs within a wider range of carrier densities than that in previous work (13, 40) which can be due to a smaller twisted angle here. Moreover, we notice that the peak value of the VHSs sharply weakens with applying larger top gate values. Similar phenomena have also been observed in other TB-WSe_2 devices (*SI Appendix*, Fig. S3). Fig. 2*B* illustrates the DOS calculated by the Tight-Binding method as a function of the normalized carrier density n/n_s and displacement field D, where the dashed black line marks the DOS peak positions. When applying a displacement field D, the DOS peak position can be effectively tuned, moving from below the half-filling to above the half-filling, and then further toward the full filling. Moreover, we notice that the strength of the DOS peak decreases monotonically across the entire range of displacement fields. To compare with our experimental results, we convert the top gate values in Fig. 2*A* into displacement fields using the formula in previous works (13, 40). We determine that applied displacement fields ranging from ∼0.24 V/nm to ∼0.5 V/nm in this 3.2° TB-WSe_2 device. Within this range, the changes in resistivity peaks of the VHSs are consistent with the changes observed in the DOS peak in the calculated phase diagram.

Furthermore, we calculate the band structure for this TB-WSe_2 device within the first moiré Brillouin zone at various displacement fields, as shown in Fig. 2*C*. The purple (black) dashed lines within each moiré Brillouin zone mark the Fermi surface at the van Hove energy in the K (K′) valley, respectively. By applying displacement fields D, the VHSs can be evidently moved within the moiré Brillouin zone. In particular, when D reaches a critical value Dc of about 0.28 V/nm, three conventional VHSs can merge into a high-order VHSs (21, 29, 32, 33, 41, 42) at the corners of the Brillouin zone marked by purple (black) points in the K (K′) valley. In this case, the corresponding density of states exhibits a power-law divergence with energy, as shown in the *Left* panel of Fig. 2*D*. As D further increases, i.e., when D equals 0.5 V/nm, the high-order VHSs move toward the center of the Brillouin zone and revert back to conventional VHSs, in which the density of states exhibits a logarithmic divergence, as illustrated in the *Right* panel of Fig. 2*D*.

Next, we focus here on the temperature dependence of the longitudinal resistivity around the half-filling correlated insulating state and VHSs regions, to elaborate on the emergence of *T*-linear dependence in resistivity measurements. Fig. 3 *A*–*D* shows the ρ as a function of n/n_s and *T* at top gate voltages of −4.3 V, −5.3 V,

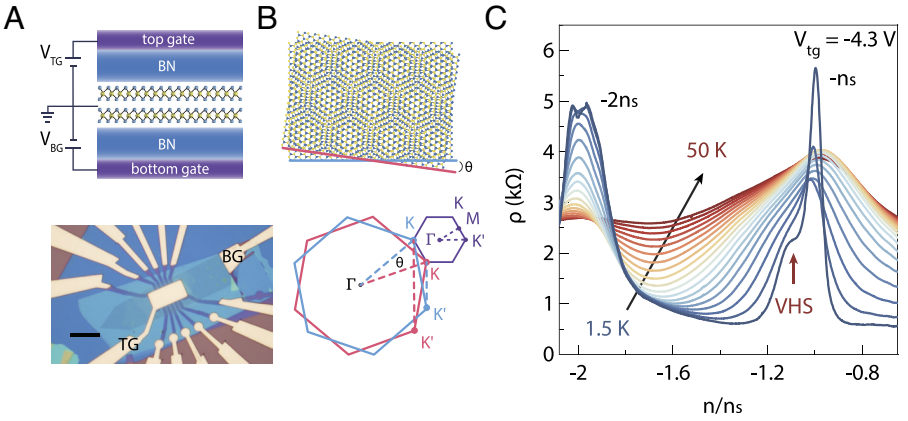

Fig. 1. Device structure and correlated insulating state in TB-WSe_2. (*A*) *Top* panel: The illustration of the TB-WSe_2 device with a dual-gate structure. *Bottom* panel: The optical image of a real TB-WSe_2 device. Black scale bar: 10 μm. "BG" and "TG" denote the back gate, and top gate respectively. (*B*) *Top* panel: real-space representation of the moiré pattern that results from a AA stacking-order between the two WSe_2 layers. *Bottom* panel: Brillouin zones of the top (red line) and bottom (blue line) layers. The resulting band structure in the moiré Brillouin zone (purple) is also displayed. (*C*) Longitudinal resistivity ρ plotted versus the normalized carrier density n/n_s at a top gate voltage V_{tg} of −4.3 V for different temperatures. It demonstrates that both the half-filling and full-filling states exhibit insulating behavior. The asymmetrical part of the half-filling peak marked by a red arrow at 1.5 K can be attributed to the VHSs being slightly shifted away from the half-filling.

Downloaded from https://www.pnas.org by UKA AACHEN INTEGR. MEDIENBEARB. MEDIZIN on January 30, 2025 from IP address 134.130.130.179.

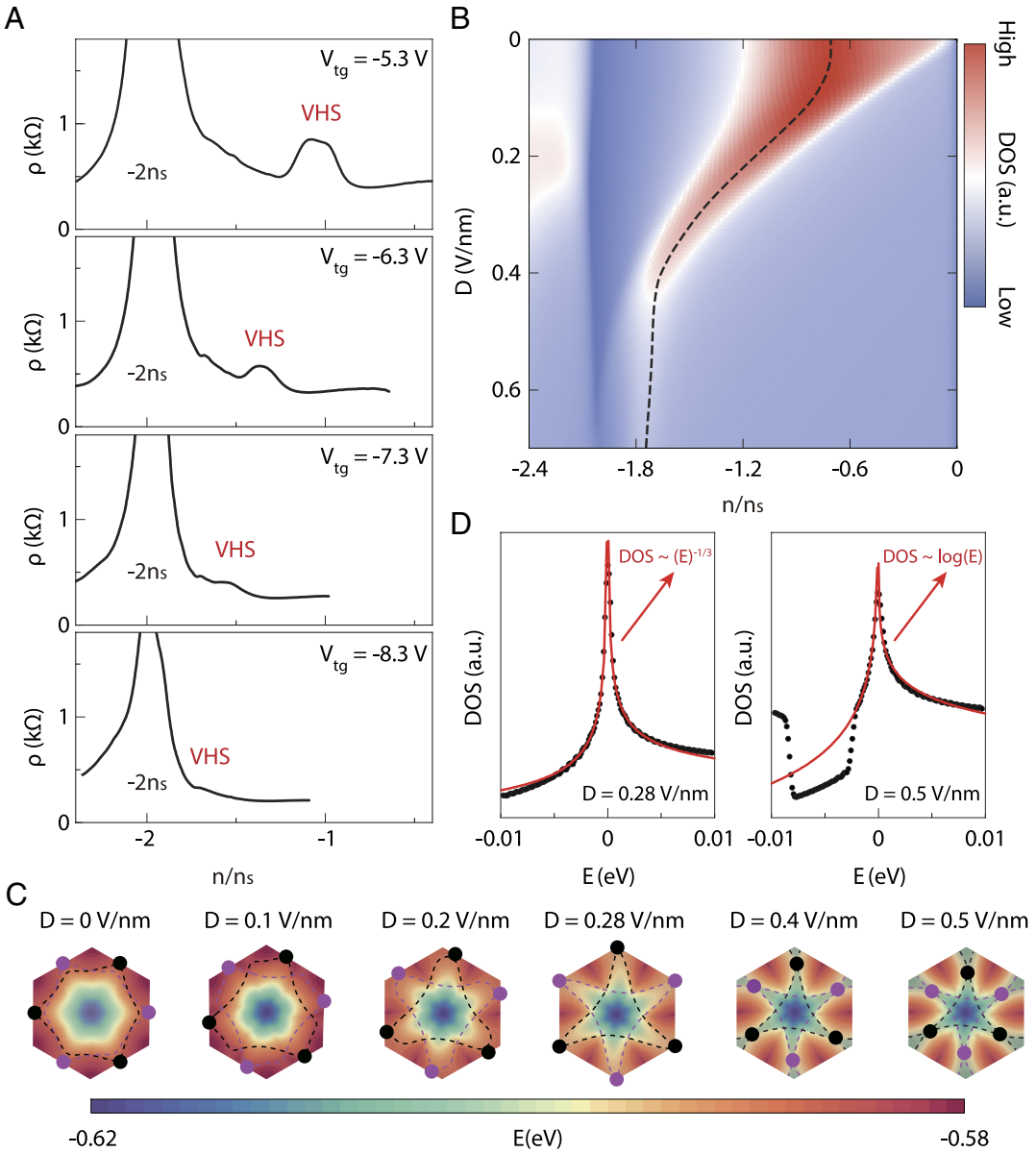

Fig. 2. Tunable van Hove singularity and the Lifshitz transition in band structure induced by displacement fields in TB-WSe_2. (*A*) Longitudinal resistivity ρ versus normalized carrier density n/n_s at various top gate voltages and T = 1.5 K. As the top gate voltage increases, the VHSs move toward the full-filling position. (*B*) The evolution of the calculated DOS with the normalized carrier density n/n_s and displacement field D, which provides a complete picture of the tunability of VHSs by displacement fields. The dashed black lines trace the position of the VHSs. (*C*) The calculated band structure within the first moiré Brillouin zone for 3.15° TB-WSe_2 device at a variety of displacement fields D. The dashed purple (black) lines mark the Fermi contour at the van Hove energy in the K (K′) valley. The purple (black) points mark VHSs in the K (K′) valley. (*D*) DOS plotted against energy E at displacement fields of 0.28 V/nm (*Left* panel) and 0.5 V/nm (*Right* panel), respectively. The red curves represent fitting curves. In the *Left* panel of *D*, at D = 0.28 V/nm, the high-order VHSs form, resulting in a power-law divergence with E. Conversely, in the *Right* panel of *D*, at D = 0.5 V/nm, the high-order VHSs revert back into conventional VHSs, exhibiting a logarithmic divergence with E.

−6.3 V, and −7.3 V, respectively, where T linear and T^2 regions around the Mott insulator and VHSs regions are marked by black dashed lines. When a top gate voltage is set to −4.3 V, we observe that the T-linear regions enclosing the half-filling correlated insulating states (marked by gray shadow), which is consistent with the previous findings of ref. 13. When the top gate voltage is increased to −5.3 V, although the Mott insulator has already collapsed due to the increasing bandwidth with increased displacement fields (40), interestingly, we can still observe a T-linear region at low temperatures within the VHSs resistivity peak region, as shown in Fig. 3*B*. As we dope away from the VHSs, T^2 regions of resistivity appear on both of its sides. Moreover, similar phenomena are also observed in Fig. 3 *C* and *D* but with a shrinking T-linear region in both carrier density and temperature ranges, which might be attributed to the weaker electron–electron or electron–phonon interaction since the bandwidth of the flat band increased further under larger displacement fields.

To clarify this change, we plot resistivity ρ versus temperature T for the doping range around the VHSs resistivity peak at top gate voltages of −5.3 V, −6.3 V, and −7.3 V, respectively, as shown in Fig. 3 *E*–*G*. Each curve corresponds to the point in the inset of the figure with the same color. In Fig. 3*E*, as we approach the VHSs resistivity peak from higher (*Left* panel) or lower doping (*Right* panel), Fermi-liquid behavior with a $R \sim T^2$ relation gradually transitions into a non-Fermi liquid behavior with a T-linear dependence. The other two plots, Fig. 3 *F* and *G*, exhibit similar tuning behavior with doping but show a slower resistivity decreasing trend with decreasing temperature at low temperatures. In this case, we also plot ρ of the VHSs against T at these three top gate voltages of −5.3 V, −6.3 V, and −7.3 V, respectively, as displayed in

Downloaded from https://www.pnas.org by UKA AACHEN INTEGR. MEDIENBEARB. MEDIZIN on January 30, 2025 from IP address 134.130.130.179.

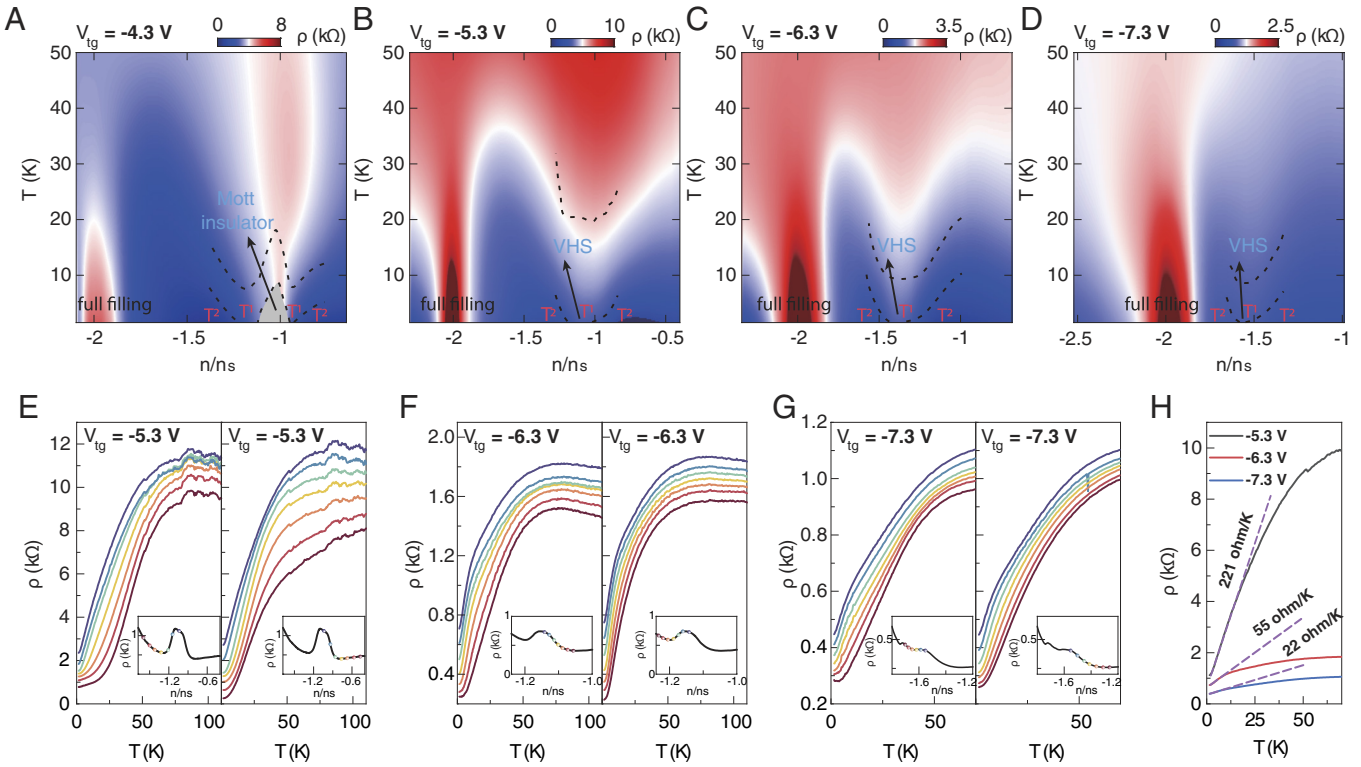

Fig. 3. Non-Fermi liquid behavior in TB-WSe_2. (*A–D*) Longitudinal resistivity ρ as a function of temperature T and normalized carrier density n/n_s at a series of top gate voltage of −4.3 V, −5.3 V, −6.3 V and −7.3 V respectively. Black dashed lines separate regions of Fermi liquid T^2 and non-Fermi liquid T resistivity. (*E–G*) ρ plot against T curves at V_{tg} of −5.3 V, −6.3 V and −7.3 V respectively. Each curve corresponds to a point in the inset figure with the same color. These curves are offset for clarity. As we approach the VHSs from higher (lower) doping, the temperature dependence of ρ changes from a Fermi-liquid behavior with a T^2 relation to a T-linear behavior. (*H*) The temperature dependence of ρ for a filling at the VHSs for three different top gate voltages of −5.3 V, −6.3 V, and −7.3 V, respectively. The purple dashed lines represent the corresponding linear fits at low T. The fitting ranges are from 1.5 K to approximately 19 K, 10 K and 7 K for V_{tg} values of −5.3 V, −6.3 V, and −7.3 V, respectively. From linear fitting, we obtained zero-temperature extrapolation values of 0.66 kΩ, 0.64 kΩ, and 0.36 kΩ, respectively, for V_{tg} values of −5.3 V, −6.3 V, and −7.3 V.

Fig. 3*H*, where the dashed purple lines indicate the corresponding fitting curves. We observe a prominent change in the value of the slope which is maximal ∼221 Ω/K at V_{tg} of −5.3 V and then sharply decreases to a small value. Based on the understanding of the band structure Fig. 2*C*, we deduce the sudden slope drop might be a consequence of large bandwidth changes as we tune through the hVHS condition. However, it is important to note that overall T-linear resistivity behavior seems to closely follow the VHS filling points, even when these filling are detuned from the Mott condition of half filling. Additionally, they prevail even when tuning into or out of the hVHS condition. This renders a mechanism for the non-Fermi liquid behavior that does not invoke quantum criticality or the exact conditions of a hVHS to be the most promising (such as VHS-enhanced phonon-scattering). Moreover, as the T-linear resistivity only persists at temperature less than a few tens of Kelvins in all our TB-WSe_2 ranging from 3 to 6 degrees (Fig. 3 and *SI Appendix*, Fig. S4), the physics underlying this mechanism may differ from that of optimally doped high-Tc cuprates, where the T-linear resistivity dependence extends to relatively high temperatures (10). Similar phenomena have also been observed in other TB-WSe_2 devices (*SI Appendix*, Fig. S4).

Finally, we apply a perpendicular magnetic field to lift the two-fold spin degeneracy in TB-WSe_2 in order to study the correlation of the T-linear behavior as the VHSs split. Fig. 4 *A* and *B* show the longitudinal resistivity ρ and Hall resistivity ρ_{xy} as a function of normalized carrier density n/n_s and temperature T at V_{tg} of −5.3 V under a magnetic field of 2 T, and a line cut of Fig. 4*A* at 1.5 K is shown in Fig. 4*C*. In Fig. 4*A*, we observe that the resistivity peak of the VHSs splits into two, which is marked as VHS_{up} and VHS_{down}, respectively. Moreover, the resistivity peaks of both VHS_{up} and VHS_{down} broaden and enhance with increasing temperatures. The corresponding ρ_{xy} displayed in Fig. 4*B* exhibits two sign changes at the lowest temperature. One of the sign changes occurs at the full filling due to the charge carriers change from hole-like to electron-like when the Fermi level passes through the band gap. The other the sign change appears at the VHS_{up} position. This is because the carrier type also changes when crossing a VHS due to the sign change of the band curvature. However, when the magnetic field splits one VHS into two, the overall carrier type depends on the details of the overlap between different carrier types determined from each VHS, which could result in only one sign change in the ρ_{xy} at one of the VHSs as we observed in experiments. Similar phenomena are also observed at other V_{tg} values in this device (*SI Appendix*, Fig. S5). Further, we plot the temperature dependence of the ρ for VHS_{up} and VHS_{down}, respectively, as shown in Fig. 4*D* together with the B = 0 T curve for comparison. We observe that each single VHS also exhibits a non-Fermi liquid behavior. Additionally, using the linear fitting, we notice that the slope values for both the VHS_{up} and VHS_{down} reduce by about half compared to the 0 T twofold degenerate case.

In conclusion, we demonstrate the tunability of the VHSs by applying displacement fields in multiple TB-WSe_2 devices via transport measurements. Our band structure calculations reveal that when the displacement field reaches a critical value of ∼0.28 V/nm in 3.2° TB-WSe_2 device, a Lifshitz transition occurs, resulting in the formation of high-order VHSs. Using displacement and magnetic fields as well as control over the filling we analyze the relevance of quantum critical points, the presence of high-order VHSs and regular VHSs for the emergence of non-Fermi liquid, linear in T resistivity. We find that the non-Fermi liquid behavior

Downloaded from https://www.pnas.org by UKA AACHEN INTEGR. MEDIENBEARB. MEDIZIN on January 30, 2025 from IP address 134.130.130.179.

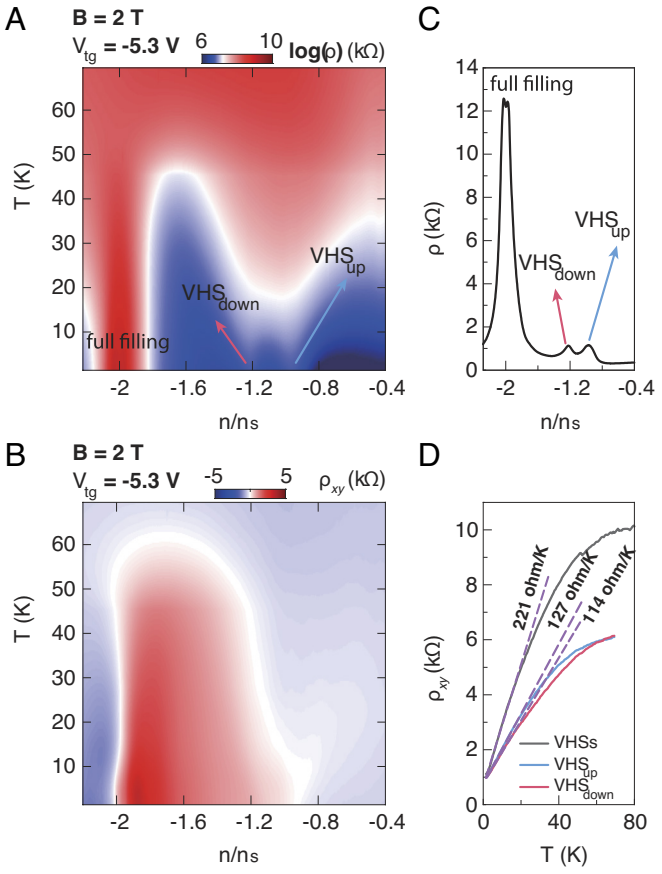

Fig. 4. Correlation of the T-linear behavior of VHSs under a small magnetic field in TB-WSe_2. (*A* and *B*) Longitudinal resistivity ρ and Hall resistivity ρ_{xy} as a function of temperature T and normalized carrier density n/n_s at a top gate voltage of −5.3 V (B = 2 T). When a magnetic field is applied, the spin degeneracy is lifted, resulting in two single VHSs denoted as VHS_{up} and VHS_{down}, respectively. (*C*) A line-cut of (A) at T = 1.5 K. (*D*) ρ plotted against temperature T at a top gate voltage of −5.3 V for the VHSs, VHS_{up} and VHS_{down}, respectively. The dashed purple lines represent the corresponding fitting lines.

seems to be induced by the presence of VHSs independent of the presence or absence of quantum criticality and seems to be agnostic of their high-order nature. Furthermore, when a small magnetic field is applied to break the spin degeneracy and split the VHSs into two, each individual VHS also shows a strong *T*-linear dependence with a twofold decrease in the slope value. Our findings underline that twisted homobilayer TMDs systems are promising platform for investigating quantum criticality and regular or high-order van Hove singularity and their interplay with high tunability. Moiré materials engineering can therefore shed light on the driving physics of non-Fermi liquids which allows us to access and simulate regimes, which could be relevant to broader quantum materials research endeavors. For example, these results should be helpful to a similar debate on the origin of non-Fermi liquid behavior and the relevance of VHSs in SRO compounds, such as Sr_2RuO_4 (43–46).

Data, Materials, and Software Availability. All study data are included in the article and/or *SI Appendix*.

ACKNOWLEDGMENTS. L. Wang acknowledges the National Key Projects for Research and Development of China (Grant Nos. 2022YFA1204700, 2021YFA1400400), National Natural Science Foundation of China (Grant No. 12074173) and Natural Science Foundation of Jiangsu Province (Grant No. BK20220066). D.M.K. acknowledges funding by the Deutsche Forschungsgemeinschaft (DFG, German Research Foundation) via Germany's Excellence Strategy–Cluster of Excellence Matter and Light for Quantum Computing (ML4Q) EXC 2004/1–390534769 and within the Priority Program SPP 2244 "2DMP"–443273985. L.X. and Q.X. acknowledge the support by the National Key Research and Development Program of China (Grant No. 2022YFA1403501) and Guangdong Basic and Applied Basic Research Foundation (Grant No. 2022B1515120020) and the Hefei National Research Center for Physical Sciences at the Microscale (KF2021003) and the Max Planck Partner group programme. The computational resources were provided by the Platform for Data-Driven Computational Materials Discovery of the Songshan Lake Materials Laboratory. K.W. and T.T. acknowledge support from the JSPS KAKENHI (Grant Numbers 21H05233 and 23H02052) and World Premier International Research Center Initiative, MEXT, Japan. We acknowledge users with Excellence Project of Hefei Science Center CAS, 2021HSC-UE007. We acknowledge support from the Max Planck-New York City Center for Non-Equilibrium Quantum Phenomena. D.A.R. and Y. He. acknowledge support from the University of Wisconsin-Madison, Office of the Vice Chancellor for Research and Graduate Education with funding from the Wisconsin Alumni Research Foundation. Open access funding provided by the Max Planck Society.

Author affiliations: [a]National Laboratory of Solid-State Microstructures, School of Physics, Nanjing University, Nanjing 210093, China; [b]Songshan Lake Materials Laboratory, Dongguan, Guangdong 523808, China; [c]College of Physics and Electronic Engineering, Center for Computational Sciences, Sichuan Normal University, Chengdu 610068, China; [d]Department of Materials Science and Engineering, University of Wisconsin, Madison, WI 53706; [e]Research Center for Electronic and Optical Materials, National Institute for Materials Science, Tsukuba 305-0044, Japan; [f]Research Center for Materials Nanoarchitectonics, National Institute for Materials Science, Tsukuba 305-0044, Japan; [g]Department of Physics and Astronomy, University of Pennsylvania, Philadelphia, PA 19104; [h]Institut für Theorie der Statistischen Physik, Rheinisch-Westfälische Technische Hochschule Aachen University and Jülich Aachen Research Alliance-Fundamentals of Future Information Technology, Aachen 52056, Germany; [i]Max Planck Institute for the Structure and Dynamics of Matter, Center for Free-Electron Laser Science, Hamburg 22761, Germany; [j]Center for Computational Quantum Physics, Simons Foundation Flatiron Institute, New York, NY 10010; and [k]Collaborative Innovation Center of Advanced Microstructures, Nanjing University, Nanjing 210093, China

Author contributions: L. Wei, D.M.K., L.X., A.R., and L. Wang designed research; L. Wei, Q.X., Q.L., Y. Huang, and W.Z. performed research; K.W. and T.T. provided hexagonal boron nitride; Y. He and D.A.R. contributed WSe2 bulk crystal; Q.X. and L.X. performed electronic structure calculations; D.M.K., L.X., and A.R. supervised the theoretical aspects of this work; L. Wei, M.C., D.A.R., D.M.K., L.X., A.R., and L. Wang analyzed data; and L. Wei, Q.X., D.M.K., L.X., A.R., and L. Wang wrote the paper.

1. L. Landau, On the theory of the fermi liquid. *Sov. Phys. JETP* **8**, 70 (1959).
2. T. Rice, Landau fermi-liquid parameters in Na and K. *Phys. Rev.* **175**, 858 (1968).
3. D. Neilson, Landau fermi liquid theory. *Aust. J. Phys.* **49**, 79–102 (1996).
4. G. Baym, C. Pethick, *Landau fermi-liquid theory: concepts and applications* (WILEY-VCH Verlag GmbH & Co. KGaA2008).
5. P. W. Anderson, *The Theory of Superconductivity in the High-Tc Cuprate Superconductors* (1997).
6. J. L. Tallon *et al.*, Critical doping in overdoped high-tc superconductors: A quantum critical point? *Phys. Status solid.* **215**, 531–540 (1999).
7. D. v. d. Marel *et al.*, Quantum critical behaviour in a high-t c superconductor. *Nature* **425**, 271–274 (2003).
8. B. Keimer, S. A. Kivelson, M. R. Norman, S. Uchida, J. Zaanen, From quantum matter to high-temperature superconductivity in copper oxides. *Nature* **518**, 179–186 (2015).
9. C. M. Varma, Linear in temperature resistivity and associated mysteries. arXiv [Preprint] (2019). https://doi.org/10.48550/arXiv.1908.05686 (Accessed 15 August 2019).
10. A. Legros *et al.*, Universal t-linear resistivity and planckian dissipation in overdoped cuprates. *Nat. Phys.* **15**, 142–147 (2019).
11. Y. Ōno, R. Bulla, A. Hewson, M. Potthoff, Critical behaviour near the metal-insulator transition of a doped mott insulator. *Eur. Phys. J. B* **22**, 283–290 (2001).
12. T. Li *et al.*, Continuous mott transition in semiconductor moire superlattices. *Nature* **597**, 350–354 (2021).
13. A. Ghiotto *et al.*, Quantum criticality in twisted transition metal dichalcogenides. *Nature* **597**, 345–349 (2021).
14. Y. Cao *et al.*, Strange metal in magic-angle graphene with near planckian dissipation. *Phys. Rev. Lett.* **124**, 076801 (2020).
15. R. L. Greene, P. R. Mandal, N. R. Poniatowski, T. Sarkar, The strange metal state of the electron-doped cuprates. *Ann. Rev. Condens. Matter Phys.* **11**, 213 (2020).
16. P. A. Lee, N. Read, Why is tc of the oxide superconductors so low? *Phys. Rev. Lett.* **58**, 2691–2694 (1987).
17. P. C. Pattnaik, C. L. Kane, D. M. Newns, C. C. Tsuei, Evidence for the van hove scenario in high-temperature superconductivity from quasiparticle-lifetime broadening. *Phys. Rev. B* **45**, 5714–5717 (1992).
18. R. Žitko, J. Bonča, T. Pruschke, Van hove singularities in the paramagnetic phase of the hubbard model: DMFT study. *Phys. Rev. B* **80**, 245112 (2009).
19. A. Shtyk, G. Goldstein, C. Chamon, Electrons at the monkey saddle: A multicritical Lifshitz point. *Phys Rev B* **95**, 035137 (2017).
20. H. Isobe, L. Fu, Supermetal. *Phys. Rev. Res.* **1**, 033206 (2019).

Downloaded from https://www.pnas.org by UKA AACHEN INTEGR. MEDIENBEARB. MEDIZIN on January 30, 2025 from IP address 134.130.130.179.

21. N. F. Yuan, H. Isobe, L. Fu, Magic of high-order van hove singularity. *Nat. Commun.* **10**, 5769 (2019).
22. N. F. Yuan, L. Fu, Classification of critical points in energy bands based on topology, scaling, and symmetry. *Phys Rev. B* **101**, 125120 (2020).
23. P. Igoshev, A. Katanin, Ferromagnetic instability in itinerant fcc lattice electron systems with higher-order van hove singularities: Functional renormalization group study. *Phys. Rev. B* **107**, 115105 (2023).
24. L. Classen, A. V. Chubukov, C. Honerkamp, M. M. Scherer, Competing orders at higher-order van hove points. *Phys. Rev. B* **102**, 125141 (2020).
25. Y. P. Lin, R. M. Nandkishore, Parquet renormalization group analysis of weak-coupling instabilities with multiple high-order van hove points inside the brillouin zone. *Phys Rev. B* **102**, 245122 (2020).
26. N. Doiron-Leyraud *et al.*, Pseudogap phase of cuprate superconductors confined by fermi surface topology. *Nat. Commun.* **8**, 2044 (2017).
27. R. S. Markiewicz, B. Singh, C. Lane, A. Bansil, High-order van hove singularities in cuprates and related high-tc superconductors. arXiv [Preprint] (2021). https://doi.org/10.48550/arXiv.2105.04546 (Accessed 10 May 2021).
28. D. V. Efremov *et al.*, Multicritical fermi surface topological transitions. *Phys. Rev. Lett.* **123**, 207202 (2019).
29. Y. T. Hsu, F. Wu, S. D. Sarma, Spin-valley locked instabilities in moire transition metal dichalcogenides with conventional and higher-order van hove singularities. *Phys. Rev. B* **104**, 195134 (2021).
30. B. Liu *et al.*, Higher-order band topology in twisted moire superlattice. *Phys. Rev. Lett.* **126**, 066401 (2021).
31. D. Guerci, P. Simon, C. Mora, Higher-order van hove singularity in magic-angle twisted trilayer graphene. *Phys. Rev. Res.* **4**, L012013 (2022).
32. H. Pan, F. Wu, S. D. Sarma, Band topology, hubbard model, heisenberg model, and dzyaloshinskii-moriya interaction in twisted bilayer wse2. *Phys. Rev. Res.* **2**, 033087 (2020).
33. J. Zang, J. Wang, J. Cano, A. Georges, A. J. Millis, Dynamical mean-field theory of moiré bilayer transition metal dichalcogenides: Phase diagram, resistivity, and quantum criticality. *Phys. Rev. X* **12**, 021064 (2022).
34. L. Wang *et al.*, One-dimensional electrical contact to a two-dimensional material. *Science* **342**, 614–617 (2013).
35. K. Kim *et al.*, van der Waals heterostructures with high accuracy rotational alignment. *Nano Letters* **16**, 1989–1995 (2016).
36. Y. Cao *et al.*, Correlated insulator behaviour at half-filling in magic-angle graphene superlattices. *Nature* **556**, 80–84 (2018).
37. L. Xian *et al.*, Realization of nearly dispersionless bands with strong orbital anisotropy from destructive interference in twisted bilayer mos2. *Nat. Commun.* **12**, 5644 (2021).
38. H. C. Movva *et al.*, High-mobility holes in dual-gated wse2 field-effect transistors. *ACS nano* **9**, 10402–10410 (2015).
39. H. C. Movva *et al.*, Density-dependent quantum hall states and zeeman splitting in monolayer and bilayer wse 2. *Phys. Rev. Lett.* **118**, 247701 (2017).
40. L. Wang *et al.*, Correlated electronic phases in twisted bilayer transition metal dichalcogenides. *Nat. Mater.* **19**, 861 (2020).
41. J. Zang, J. Wang, J. Cano, A. J. Millis, Hartree-fock study of the moire hubbard model for twisted bilayer transition metal dichalcogenides. *Phys. Rev. B* **104**, 075150 (2021).
42. Z. Bi, L. Fu, Excitonic density wave and spin-valley superfluid in bilayer transition metal dichalcogenide. *Nat. Commun.* **12**, 642 (2021).
43. A. Tyler, A. Mackenzie, S. NishiZaki, Y. Maeno, High-temperature resistivity of sr 2 ruo 4: Bad metallic transport in a good metal. *Phys. Rev. B* **58**, R10107 (1998).
44. A. Husain *et al.*, Coexisting fermi liquid and strange metal phenomena in sr2ruo4. arXiv [Preprint] (2020). https://arxiv.org/abs/2007.06670v1 (Accessed 3 July 2020).
45. A. Hunter *et al.*, The fate of quasiparticles at high-temperature. arXiv [Preprint] (2023). https://doi.org/10.48550/arXiv.2308.02313 (Accessed 4 August 2023).
46. J. B. Hauck, S. Beck, D. M. Kennes, A. Georges, O. Gingras, Competition between d-wave superconductivity and magnetism in uniaxially strained sr2ruo4. arXiv [Preprint] (2023). https://doi.org/10.48550/arXiv.2307.10006 (Accessed 19 July 2023).

Downloaded from https://www.pnas.org by UKA AACHEN INTEGR. MEDIENBEARB. MEDIZIN on January 30, 2025 from IP address 134.130.130.179.